Clutter Filter Wave Imaging

Sebastien Salles, Lasse Løvstakken, Svein Arne Aase, Tore Grüner Bjåstad, and Hans Torp

***Abstract*— The elastic properties of human tissue can be evaluated through the study of mechanical wave propagation captured using high frame rate ultrasound imaging. Methods such as block-matching or phase-based motion estimation have been used to estimate the displacement induced by the mechanical waves. In this paper, a new method for detecting mechanical wave propagation without motion estimation is presented, where the motion of interest is accentuated by an appropriate clutter filter. Thus, the mechanical wave propagation will directly appear as bands of the attenuated signal moving in the B-mode sequence and corresponding anatomical M-mode images. While only the locality of tissue velocity induced by the mechanical wave is detected, it is shown that the method is more sensitive to subtle tissue displacements when compared to motion estimation techniques. The technique was evaluated for the propagation of the pulse wave in a carotid artery, mechanical waves on the left ventricle, and shear waves induced by radiation force on a tissue-mimicking phantom. The results were compared to tissue Doppler imaging (TDI) and demonstrated that clutter filter wave imaging (CFWI) was able to detect the mechanical wave propagating in tissue with a relative temporal and spatial resolution 30% higher and a relative consistency 40% higher than TDI. The results showed that CFWI was able to detect mechanical waves with a relative frequency content 40% higher than TDI in a shear wave imaging experiment.**

***Index Terms*— Clutter filter, mechanical wave propagation, pulse wave (PWV), shear waves, ultrafast imaging.**

I. Introduction

In THE last 20 years, the advent of high frame rate ultrasound imaging has allowed the study of high-speed physiological phenomena occurring in the human body. Concerning tissue imaging and characterization, improvements in high frame rate ultrasound imaging have permitted the visualization and thereby measurements of the elastic properties [1].

Tissue elasticity imaging can be divided into two different approaches. The first approach consists of studying the propagation of artificially induced shear waves. This approach was first developed with a mechanical vibrator [2], [3] able to induce low-frequency vibration of a few hundred hertz. Later, another approach called shear wave elasticity imaging (SWEI), based on the use of shear acoustic waves remotely induced by the radiation force of a focused ultrasonic beam, and able to induce mechanical waves at several kilohertz, has been introduced [4]–[6] and applied to different pathologies [7]–[10]. The second approach consists of studying the propagation of mechanical waves induced naturally by the human body itself. With the development of pulse wave (PWV) imaging, the velocity of the so-called PWV can be estimated, providing a quantitative evaluation of arterial stiffness [11]–[16]. In the domain of cardiac imaging, the velocities of different mechanical waves propagating along the heart wall have been studied [17]–[23]. More recently, a new approach using the permanent physiological noise of the human body, called passive elastography, has been developed [24].

All approaches involve two major steps [25] for the visualization and the velocity estimation of the mechanical waves: tissue motion estimation and mechanical wave velocity estimation. Phase-based and RF/B-mode cross correlation (CC) methods are the two main techniques used to estimate the beam axis motion generated by mechanical waves [25]. Tissue Doppler imaging (TDI) estimates the tissue motion in the beam direction by estimating the lag-one autocorrelation of the temporal IQ signals [26]. CC techniques, such as normalized CC, the sum of squared differences, and the sum of absolute differences [27], [28], are based on locating the corresponding segment of data from the current frame in consecutive frames. Each approach has its advantages and disadvantages. TDI is generally recognized as a method sensitive to beam angle and needs a high frame rate to avoid aliasing [29]. However, TDI techniques provide inherent subpixel displacement estimation and are computationally inexpensive [29]. Two-dimensional CC techniques are not sensitive to beam angle and provide the estimation of larger displacements without aliasing. However, even though fast CC techniques have been developed [30], the CC methods require substantially more processing time and require additional subpixel displacement estimation [11].

Since knowing the absolute tissue velocity is not required for the estimation of wave velocity propagation, we propose a technique able to detect the mechanical wave propagation without tissue velocity estimation. Our method consists of applying a carefully designed temporal clutter filter to the IQ data, where the transition band is used to accentuate the desired band of tissue velocities. The wave propagation is then visible as low-intensity bands moving in the resulting B-mode sequences and can be measured in the corresponding anatomical M-mode display as for previous approaches.

The objective of this paper is to present this clutter filter wave imaging (CFWI) approach, to evaluate it on three mechanical wave applications, and to compare the results with TDI. Initially, CFWI is evaluated for a tissue-mimicking phantom where shear waves were induced by radiation forces. The detection of the mechanical waves was quantitatively

Manuscript received February 27, 2019; accepted June 12, 2019. Date of publication June 20, 2019; date of current version August 26, 2019. This work was supported in part by the Center for Innovative Ultrasound Solutions (CIUS), a center for research-based innovation, and in part by the Research Council of Norway. *(Corresponding author: Sebastien Salles.)*

S. Salles, L. Løvstakken, and H. Torp are with the Department of Circulation and Medical Imaging, Norwegian University of Science and Technology, 7491 Trondheim, Norway (e-mail: sebastien.salles@ntnu.no).

S. A. Aase and T. G. Bjåstad are with GE Vingmed Ultrasound, 3183 Horten, Norway.

Digital Object Identifier 10.1109/TUFFC.2019.2923710

achieved through the estimation of the group velocity and shear wave dispersion curves. Then, CFWI was tested *in vivo* in two experiments with healthy volunteers. First, the detection of the forward, backward, and dicrotic notch waves was quantitatively achieved, and the effects of the spatiotemporal filter and CFWI cutoff frequency were evaluated in data from the carotid artery. Second, two naturally occurring mechanical waves, induced at the aortic valve closure (AVC) and the atrial contraction during (a′ waves), were detected and measured in the left ventricle.

In the following, Section II presents the CFWI principle and method. Then, Section III briefly reviews the comparative approach, and the mechanical wave velocity estimation method before presenting the three different experiments performed in this work. Finally, the results are shown in Section IV and are discussed in Section V.

II. Clutter Filter Wave Imaging

A. Principle

Clutter rejection filtering (CRF) techniques were initially used in RADAR applications to suppress received signal from stationary targets (clutter) in order for the detection of moving targets [31]. In ultrasound medical imaging, CRF is similarly necessary and still a challenge in blood flow imaging [32], and it is also partly used in TDI to avoid underestimation of tissue velocities. Several types of filters have been proposed, such as finite impulse response filter, infinite impulse response filter, and polynomial regression filter [33]–[35]. Due to the inherent nonstationarity of tissue motion, several data adaptive filters have been proposed such as the down-mixing method and the eigenvector regression filter which takes into account the tissue velocity and acceleration [36]–[38].

CRF is used mostly for the complete attenuation of the tissue motion. Here, CRF is used to reject or attenuate only a range of tissue velocities partially. In this way, the aim is to attenuate only the tissue velocities induced by the mechanical wave propagation. These waves will then be visible as darker/gray bands in the B-mode sequences following the propagation of the mechanical wave. This principle is depicted in Fig. 1. Moreover, this technique also attenuates the stationary component in the manner of pulse inversion techniques [24], [25].

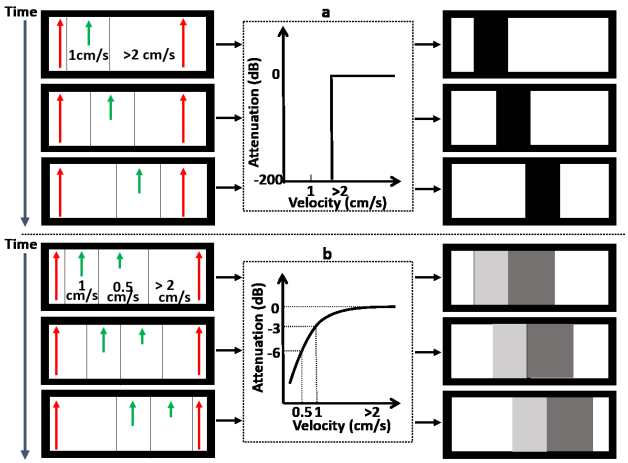

Fig. 1. Principle of clutter filtering wave imaging. (a) Medium with two axial velocities (1 cm/s in green and >2 cm/s in red) is filtered with an ideal high-pass filter with a cutoff velocity at 2 cm/s. The resulting medium will contain a fully attenuated (black) region, which corresponds to the removed 1 cm/s velocity. (b) Medium with three axial velocities (1 and 0.5 cm/s in green and >2 cm/s in red) is filtered with a conventional high-pass filter with a cutoff velocity >2 cm/s. The resulting medium will contain two partially attenuated (gray) regions corresponding to the attenuated 1 and 0.5 cm/s velocities. If those velocities propagate along the medium, the black/gray regions will also propagate.

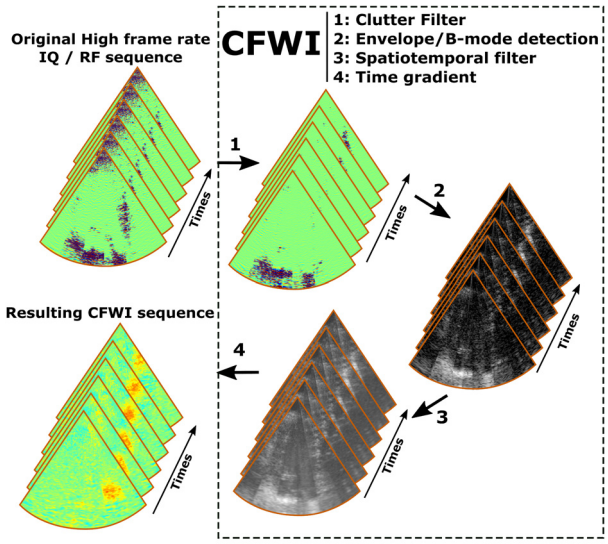

Fig. 2. CFWI method. The processing is depicted using a left ventricular example. The IQ or RF sequence is clutter filtered using a high-pass filter (1). After envelope detection (2), the resulting sequences are spatiotemporally filtered (3), and finally differentiated in time (4).

B. Clutter Filter Wave Imaging Method

CFWI consists of four main steps, as shown in Fig. 2.

1) Clutter Filter: CFWI uses the stop and transition band of the clutter filter to attenuate the Doppler frequencies corresponding to the tissue velocities of the wave propagation of interest. Depending on the width of the transition region and the stopband attenuation, the filter will attenuate a broad or more narrow range of tissue Doppler frequencies. These provide a mechanism for selecting the bandwidth of wave propagation velocities of interest. Several filter designs can be used, here the same causal first-order high-pass Butterworth filter was used for all three experiments with different cutoff frequencies corresponding roughly to the maximum tissue velocity (Fig. 3). The filter was applied in the time dimension. The normalized cutoff frequency fc_n is defined as

$$fc_n = V_c / \upsilon\mathrm{Nyq} \tag{1}$$

with

$$\upsilon\mathrm{Nyq} = \frac{c_0 \times \mathrm{FPS}}{4 f_0} \tag{2}$$

and

$$fc = fc_n \times \mathrm{FPS}/2 \tag{3}$$

where V_c is the cutoff velocity, to be chosen according to the tissue velocity of the studied medium, c_0 is the speed of

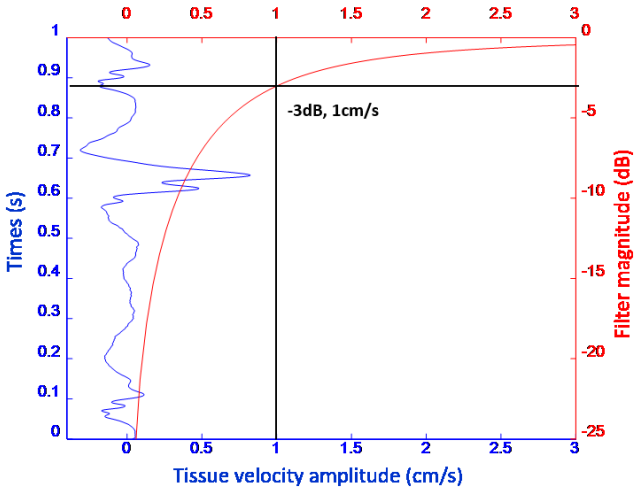

Fig. 3. Example of a high-pass filter used for CFWI. Blue curve: tissue velocity of a carotid wall. Red curve: magnitude of the high-pass filter. In this example, the cutoff frequency of a first-order Butterworth filter was set at 68 Hz in order to attenuate the velocity under 1 cm·s^{-1}.

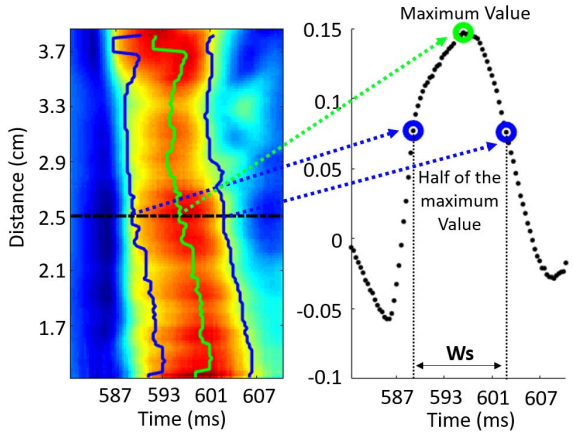

Fig. 4. Parameter estimation. The figure shows an example of how the parameters of comparison were calculated for the estimation of the PWV in the carotid artery, after estimating the maximum value of the slope (green point). The temporal interval associated with the FWHM of the tissue velocities for the mechanical wave, averaged over a spatial ROI. SNR was defined as the ratio of the mean and the standard deviation of the tissue velocities comprised within the FWHM and the ROI.

sound, FPS is the frame rate, f_0 the transmit frequency, vNyq the Nyquist velocity, and fc is the cutoff frequency in hertz.

2) Envelope and B-Mode Detection: The resulting RF sequences were envelope detected using the absolute value of the Hilbert transform, while IQ sequences were envelope detected using the absolute value of the IQ data. A logarithmic compression can be performed to extract the B-mode image.

3) Spatiotemporal Smoothing: Spatiotemporal averaging (low-pass filter) of the resulting sequences can be used to increase the signal-to-noise ratio (SNR) of the data, reducing the variance in the following mechanical wave slope estimation. While this step is necessary for the detection of mechanical waves using a motion estimation method, it will be shown that CFWI can detect waves without it.

4) Time Gradient: The resulting sequence is differentiated in time to recover an image of the tissue acceleration. Because the foot of the mechanical wave is defined as the inflection point, at which the temporal derivative of the velocity (i.e., wall acceleration) attains its maximum before the peak velocity, this last step allows better detection of the tissue velocity propagation for visualization of mechanical waves and estimation of the wave velocities.

C. Comparison Method

The presented technique was compared to the acceleration map obtained by a similar TDI approach. The comparative method was implemented by taking the phase of the spatiotemporal filtered lag-one autocorrelation of the IQ signal as follows:

$$\hat{V} = \frac{\angle \hat{R}_x(1) \times v\text{Nyq}}{\pi} \tag{4}$$

where $\angle \hat{R}_x(1)$ represents the phase angle of the spatiotemporal filtered autocorrelation with lag-one.

In order to realize a fair comparison, and because the TDI technique typically needs spatial and temporal low-pass filtering, the same filters and filter parameters were used for both methods. The spatiotemporal filtering was applied before the angle detection for TDI, and after the clutter filter for the CFWI. TDI and CFWI were performed in consecutive frames on entire sequences. Spatiotemporal acceleration maps (Figs. 6, 8, and 12) were extracted by averaging a region of interest (ROI) along the thickness of the wall for the carotid and cardiac experiments and the depth for the shear waves imaging experiment. In this paper, both methods were compared for three different parameters.

1) Ws: The temporal full-width at half-maximum (FWHM) of the tissue velocities associated with a mechanical wave, averaged over a spatial ROI.
2) SNRs: SNR was defined as the ratio of the mean and the standard deviation of the tissue velocities within the FWHM and the ROI.

$$\text{SNRs} = \frac{\mu}{\sigma} \tag{5}$$

where μ and σ are, respectively, the average amplitude and the standard deviation of the signal in the band defined by the two time samples found previously [Fig. 4 (blue line)].
3) In addition, the precision of the mechanical wave velocities was obtained by calculating the standard deviation over several cardiac cycles in a single subject.

Finally, for the shear wave experiment, the frequency content of the dispersion curve was used qualitatively to compare both methods using the method from [39].

D. Experiments

CFWI was evaluated with three different experiments; for the detection of shear waves in a tissue-mimicking phantom, PWVs in the carotid artery, and mechanical waves in the left ventricle. Written consent was obtained from each volunteer.

1) Shear Wave Imaging in a Tissue-Mimicking Phantom: For data acquisition, a Vantage 256 system (Verasonics, Kirkland, WA, USA) and L11-4v probe (128 elements, driven

at 4.8 MHz, 0.3-mm pitch, 28-mm elevation focus) were used. The system allows switching between the acoustic radiation force impulse (ARFI) sequence for the generation of shear waves and an ultrafast imaging sequence to image the rapid shear wave propagation. Only 64 elements were used for the transmission of ARFI pulse of 100 μs, while the ultrafast imaging was realized by transmitting plane waves with 128 elements, at 10 kHz and with a pulselength of 0.2 μs. A homogeneous tissue-mimicking phantom made of poly(vinyl alcohol) (PVA) was used. CFWI was performed with a cutoff frequency set at 468 Hz in order to attenuate tissue velocities below 7.5 cm/s (corresponding to the maximum tissue velocity found by TDI). CFWI was performed with and without logarithmic compression according to the desired outcome. A logarithmic compression was used for the visualization of the shear wave and the estimation of the group velocity, while no log compression was used for the estimation of the dispersion curve, to not disturb the linearity of the results. For the same reason, the estimation of the dispersion curve was achieved without any smoothing method. For the group velocity estimation, the spatiotemporal acceleration maps were smoothed with a moving average filter of four time samples and two spatial samples (0.4 ms $\times$ 0.3 mm). The local assessment of group velocity was achieved by estimating the time of flight between two time points during the shear wave propagation. The time-of-flight estimation is based on the 1-D CC of the local spatiotemporal acceleration map corresponding at ROI at a certain depth. This technique is similar to the method used in [39].

2) Pulse Wave Velocity Estimation in the Carotid Artery: The same setup as used for the shear waves experiment was also used in this experiment. Only a single plane wave insonification was transmitted for the reconstruction of one image, reaching 3000 FPS. The raw RF data was beamformed using Stolt's method for plane wave imaging [40]. The longitudinal (long axis) view of the right common carotid artery of one healthy subject was scanned during 3 s and 4 times to include 12 cardiac cycles. CFWI was performed with a cutoff frequency set at 68 Hz to attenuate the tissue velocity below 1 cm/s (corresponding to the maximum tissue velocity found with TDI). No logarithmic compression was used in this experiment, only envelope detection. The spatiotemporal acceleration maps were smoothed with a moving average filter of 10 time samples per five spatial samples (3 ms $\times$ 1.5 mm). The foot of PWV was defined as the inflection point, at which the temporal derivative of the velocity (i.e., wall acceleration) attains its maximum before the peak velocity was extracted and was plotted against the distance traveled by the PWV. A linear regression fit was applied to the time–distance plot. The wave velocities were then calculated as the reciprocal of the linear regression slope. In order to provide an indicator of the robustness, the average and standard deviation value of each wave velocities (forward, reflected, and dicrotic notch waves) were calculated from the 12 consecutive cardiac cycles.

3) Mechanical Wave Detection in the Left Ventricular Myocardium: For data acquisition, a locally modified Vivid E95 scanner (GE Vingmed Ultrasound, Horten, Norway) with a 1.5D M5Sc-D cardiac probe with a 3.5-MHz central frequency was used. Ultrafast imaging was achieved by transmitting six plane waves ($-35°$ to $35°$) to cover the ROI (no compounding), resulting in 820 FPS. The left ventricle of one healthy subject was scanned in the four-chamber view during 2 s and three times to produce six full cardiac cycles. CFWI was performed with a cutoff frequency set at 114 Hz in order to attenuate the tissue velocities below 2.5 cm/s. A logarithmic compression was used in this experimentation. The spatiotemporal acceleration maps were smoothed with a moving average filter of 30 time samples and 10 spatial samples (36 ms $\times$ 4 mm). The mechanical wave velocities were estimated using the same method as used for the estimation of the PWV velocity.

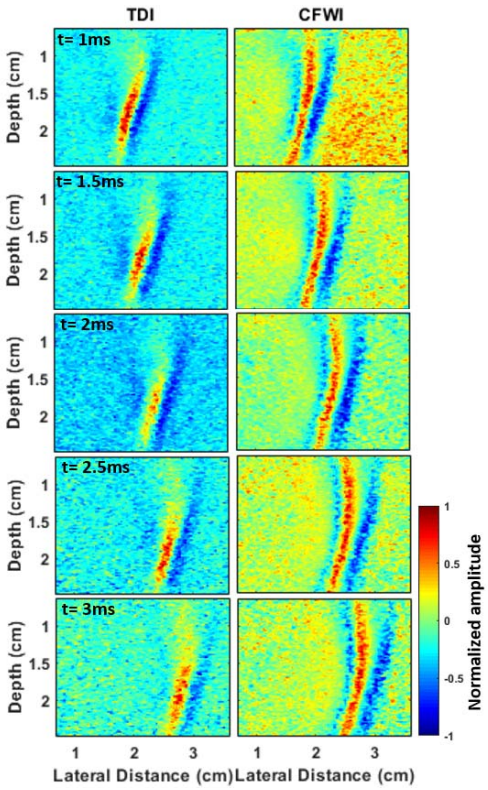

Fig. 5. Visualization of shear wave propagation in the tissue-mimicking phantom. The propagation of the shear wave is more accessible using CFWI than TDI.

III. Results

A. Shear Waves in a Tissue-Mimicking Phantom

The results obtained with TDI and CFWI following a single push are shown in Fig. 5. The acceleration amplitudes were normalized in order to compare both methods. The shear wave is visible for both methods; however, its propagation is more visible with CFWI along the depth and the time axes. Indeed, CFWI seems to be less affected by the wave attenuation compared to TDI, and so we are able to detect the shear wave more clearly along the sequence.

This difference is also visible in Fig. 6, where the spatial average value (in depth), over the ROI shown in Fig. 5, is depicted for the TDI, CFWI, and CFWI without a logarithmic compression. CFWI results without logarithmic compression are more similar to the TDI results and degrade due to the wave attenuation. However, the red curves representing the amplitude of the corresponding spatiotemporal map at different

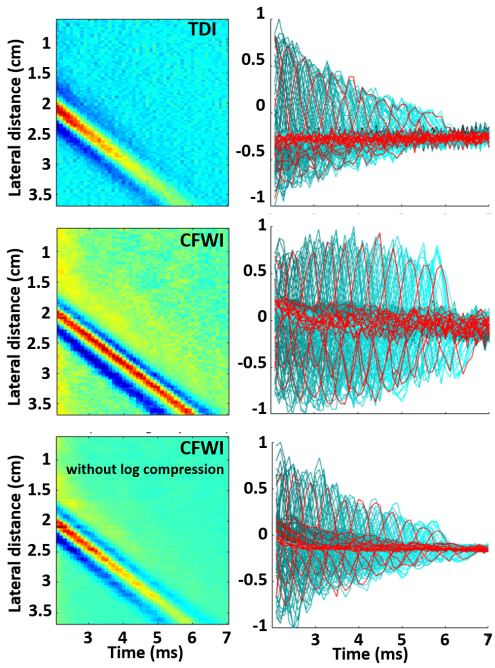

Fig. 6. Normalized spatiotemporal maps obtained with TDI, CFWI, and CFWI without a logarithmic compression. On the right of each case, the blue curve corresponds to each spatial sample along the time. In order to better visualize the differences, one sample for every 10th sample is depicted in red.

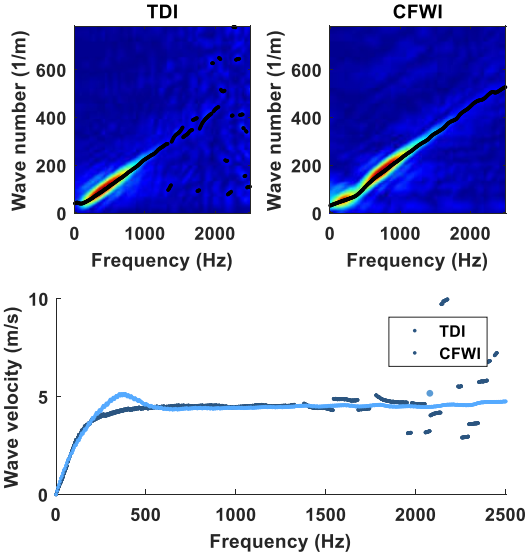

Fig. 7. k-space and dispersion curve for shear waves propagating in a tissue-mimicking phantom. Top: k-space representations of the shear waves detected with TDI and CFWI. Bottom: Respective dispersion curves.

lateral distances along the time showed that the shear waves are described better for the CFWI methods.

The average shear wave velocities estimated, over the ROI shown in Fig. 5, with TDI, CFWI, and CFWI without logarithm compression, in m·s^{-1}, are 4.22 ± 1.03 and 4.34 ± 0.72, and 4.34 ± 0.72 m·s^{-1}, respectively.

Fig. 7 shows the dispersion curve estimated using TDI and CFWI. Both curves are very similar; however, two differences can be observed. First, a bump is visible, around 400 Hz, in the CFWI results. Second, CFWI seems to be able to detect the shear waves up to 2.5 kHz, while TDI detects them up to 1.5 kHz.

TABLE I

NATURAL MECHANICAL WAVES ON CAROTID ARTERY TDI VERSUS CFWI

Wall	Method	Ws (ms)	SNRs (dB)	Forward wave (m/s)	Reflected wave (m/s)	Dicrotic notch (m/s)
Upper	TDI	12.4	5.4	4.40 ± 0.62	2.63 ± 0.54	5.93 ± 0.70
Upper	CFWI	**9.6**	**5.9**	4.34 ± **0.24**	2.10 ± **0.24**	5.90 ± **0.59**
Lower	TDI	10.8	6.2	5.89 ± 0.9	6.21 ± 1.33	6.45 ± 0.85
Lower	CFWI	**7.7**	**7.7**	5.49 ± **0.44**	5.58 ± **0.25**	6.29 ± **0.6**

B. Pulse Wave Velocities in the Carotid Artery

An example of the results obtained with TDI and CFWI for one cardiac cycle in the lower wall is depicted in Fig. 8(a). The results show that both techniques can detect PWVs. Indeed, the forward, reflected, and dicrotic notch waves are clearly described by both methods. However, qualitatively, CFWI seems to detect the mechanical waves with a better temporal resolution of the slope, which could allow for a more accurate mechanical wave velocity estimation. Moreover, the results show that CFWI can, additionally, detect the zero crossing of velocities using the acceleration map.

To quantify the differences, the average mechanical wave velocities, Ws, and SNRs, estimated over 12 cardiac cycles and the corresponding standard deviations are depicted in Table I. First, the results show that both methods gave the same average values for the forward, reflected, and dicrotic notch waves, which again were in agreement with findings in the literature [13], [15], [41]. However, the standard deviation estimated over 12 cardiac cycles is better for the CFWI. Also, the results show that CFWI allowed better Ws than TDI while keeping the SNRs in the same order of magnitude.

Furthermore, Fig. 8(b) illustrates that CFWI does not need any spatiotemporal averaging compared to TDI to detect the different mechanical waves in this example.

By mapping the CFWI results, the mechanical wave propagation can be visualized directly on the B-mode sequences. An example of the mechanical wave visualization on the carotid artery is shown in Fig. 9. The propagation of PWV was here more accessible using CFWI than TDI.

The effect of the spatiotemporal averaging filter on the mechanical wave velocity estimation is depicted in Fig. 10. The estimated mechanical wave velocity increases with the size of the spatiotemporal averaging windows.

The velocity of the forward and dicrotic notch waves, propagating in the carotid artery, was estimated with different cutoff frequencies from 30 to 95 Hz. The results are shown in Fig. 11, estimated for one single cardiac cycle. The average value over the different cutoff frequencies and the corresponding standard deviation for the forward waves and dicrotic notch waves are, in m·s^{-1}, 4.61 ± 0.15 and 5.19 ± 0.18.

C. Natural Mechanical Waves in the Left Ventricle

An example of the results obtained with TDI and CFWI for one cardiac cycle is depicted in Fig. 12. Five different tissue velocity propagations were found and indicated in (1)–(5) of Fig. 12. First, concerning the septal wall, both methods

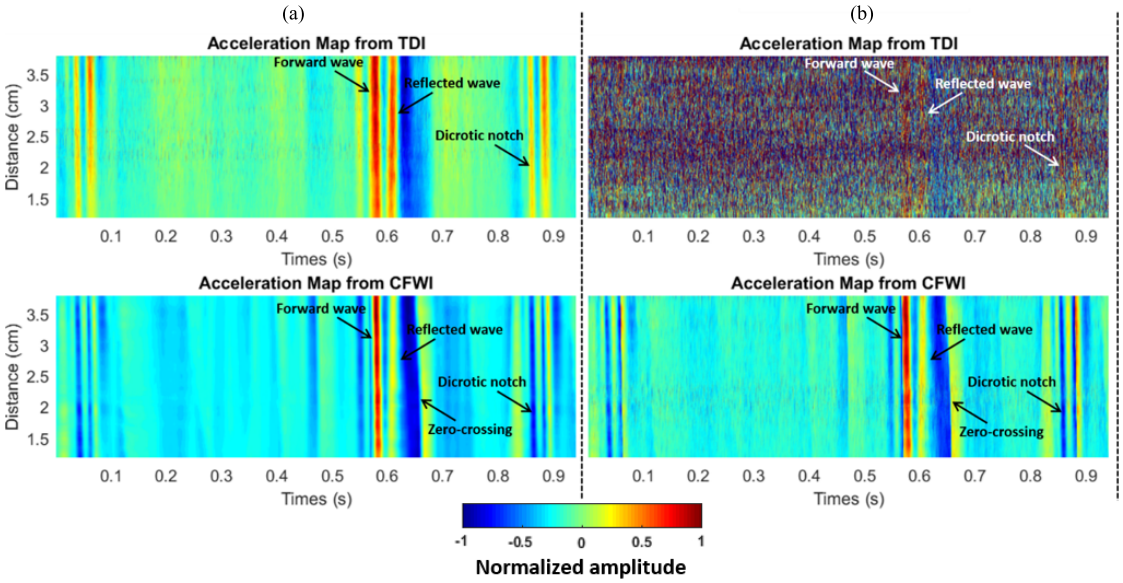

Fig. 8. Normalized spatiotemporal maps obtained with TDI and CFWI. (a) Same moving average filter was used for both methods. The forward, reflected, and dicrotic notch waves are visible using both methods. (b) Same spatiotemporal map computed without using any moving average filter. The three above mentioned waves are still clearly visible using CFWI. As CFWI is not able to differentiate a positive or negative velocity, a swap in color can be visible between TDI and CFWI (dicrotic notch). This phenomenon is discussed in Section IV.

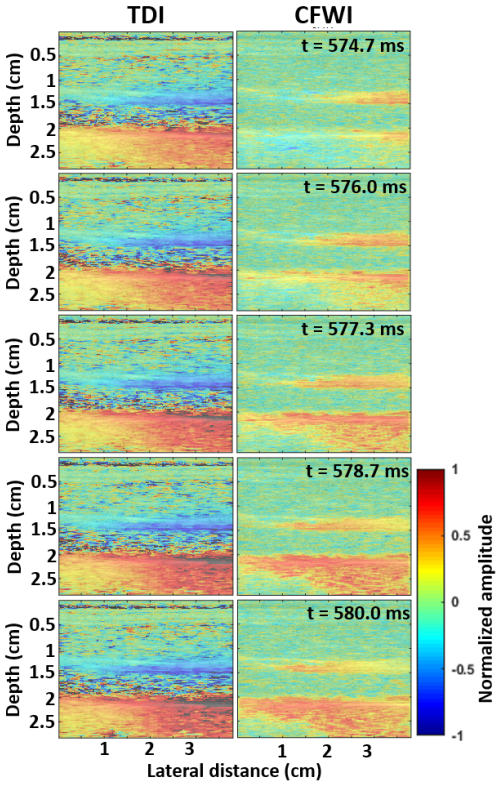

Fig. 9. Visualization of PWV propagation on the carotid artery. The accelerations obtained with TDI and the results obtained with CFWI are mapped on the B-mode sequences.

showed equivalent results, the five propagation events were well detected with approximatively the same speed. Nevertheless, the different slopes corresponding to the propagation of velocity are more pronounced with the CFWI method, especially in the apical region. Concerning the lateral wall, CFWI exhibited improved depiction of all mechanical wave propagation in this example, which is clearly shown in Fig. 12.

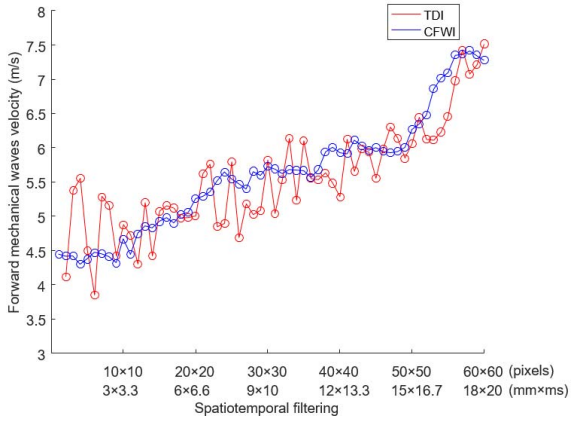

Fig. 10. Effect of the spatiotemporal averaging window on the estimated PWV velocity propagating for the carotid artery.

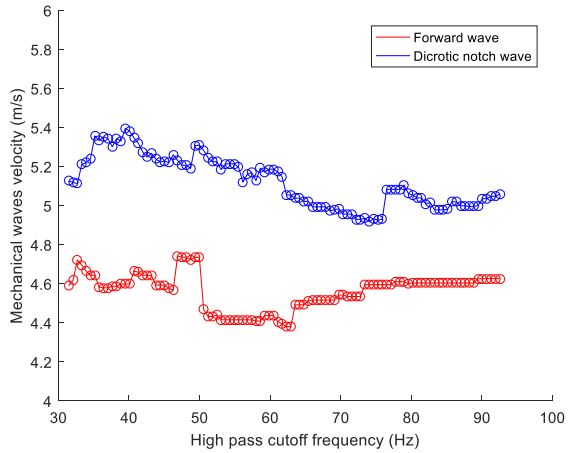

Fig. 11. Velocity of the forward and dicrotic notch waves propagating on a carotid artery according to CFWI cutoff frequency ranging from 30 to 95 Hz.

The average a′ [Fig. 12 (2)] and AVC [Fig. 12 (5)] mechanical wave velocities, Ws, and SNRs, estimated over six cardiac

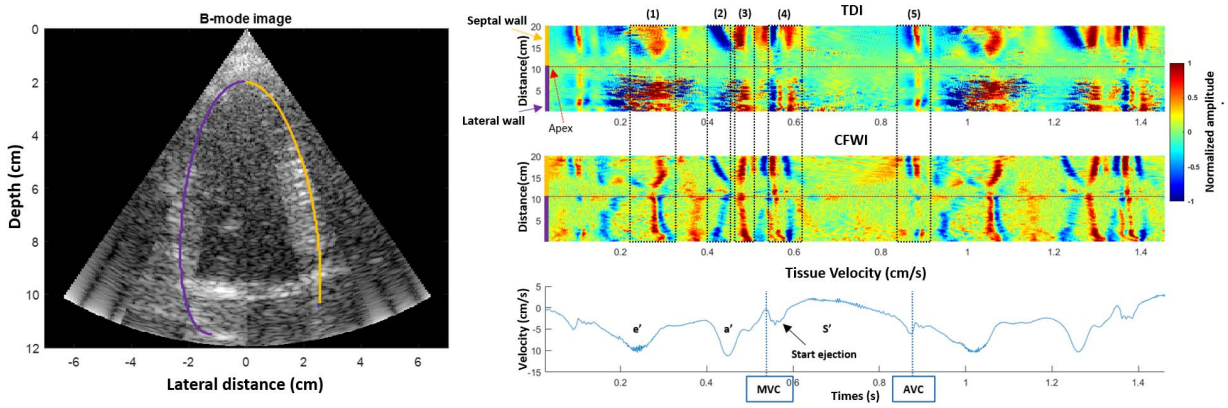

Fig. 12. Spatiotemporal maps obtained with TDI and CFWI. Left: example of the left ventricle image used is shown. Violet and yellow lines: anatomical M-mode used to extract the spatiotemporal acceleration map. Both parts of the wall are indicated on the acceleration maps. Right: both acceleration maps obtain with TDI and CFWI are depicted. Bottom right: one tissue velocity curve located at the mid-septal wall. The numbers (1)–(5) indicate different velocity propagation events found in these maps. Because CFWI is not able to differentiate a positive or negative velocity, a swap in color can be visible between TDI and CFWI (4). This phenomenon is elaborated in Section IV.

TABLE II
NATURAL MECHANICAL WAVES ON THE LEFT VENTRICLE TDI VERSUS CFWI

Methods	Ws (ms)	SNRs (dB)	a' (m/s)	AVC (m/s)
TDI	5.69	**2.59**	1.77 ± 0.25	5.12 ± 0.61
CFWI	**3.36**	2.65	1.66 ± **0.14**	5.37 ± **0.44**

cycles, and the corresponding standard deviations are given in Table II.

First, the results show that both methods return the same average values for both waves, which were in agreement with findings in the literature [19], [21], [22]. However, the standard deviation estimated over six cardiac cycles is better for the CFWI. Furthermore, the results show that CFWI allowed better Ws than TDI while keeping the SNRs in the same order of magnitude. By mapping the CFWI results, the mechanical wave propagation can be visualized directly on the B-mode and anatomical M-mode sequences. An example of the mechanical wave visualization on the left ventricle is shown in Fig. 13. The propagation of the a′ wave is more accessible using CFWI than TDI for both walls.

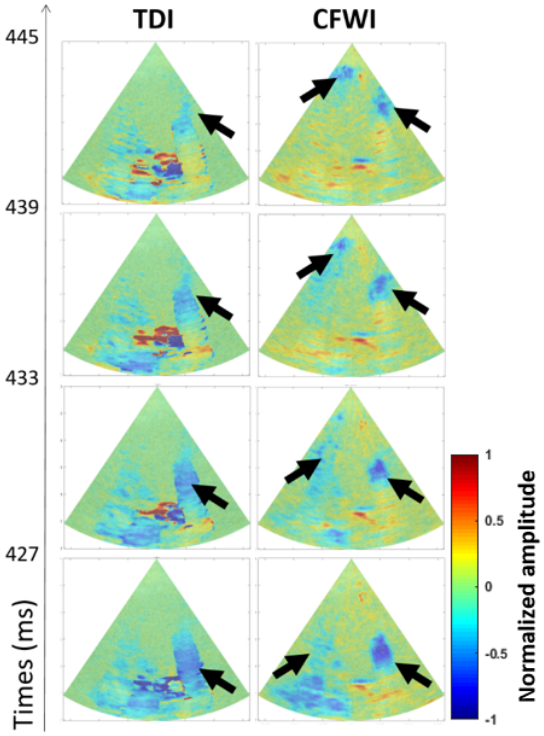

Fig. 13. Visualization of a mechanical wave propagation found in (2) of Fig. 12 on the left ventricle. The accelerations obtain with TDI and the results obtain with CFWI are mapped on the B-mode sequences.

IV. DISCUSSION

In this paper, a new method for detecting the propagation of mechanical waves in tissue without motion estimation is presented. Motion estimation methods such as TDI has the advantage of extracting two linked parameters, namely, the velocity of the tissue and the locality of the tissue velocity. Nevertheless, even if the tissue velocities themselves could be clinically useful, only the locality of the tissue velocity is needed to be able to detect the mechanical waves and estimate the propagation velocity. The presented method, named CFWI, was used to detect the locality of the tissue velocities induced by the mechanical waves, which can be used afterward to extract other information about tissue characteristics.

In CFWI, the transition band of a clutter filter attenuates the desired tissue-Doppler frequencies; in this manner, the propagation of the corresponding velocity band will be visible as an attenuated region in the resulting B-mode sequences, propagating with the tissue displacements caused by the mechanical wave. Consequently, the transition band of the clutter filter can be set according to the range of velocities to be accentuated. In this paper, we chose the maximum tissue velocity as a parameter for the CFWI process to detect all the mechanical waves, even if they induced motion with different amplitudes and even if there is a general motion on the top of the wave motion. The high-pass cutoff frequency and the order of the filter were chosen empirically for this purpose. Nevertheless, it is possible to attenuate only a smaller range

of tissue velocities by increasing the order of the filter and by using an adapted cutoff frequency.

First, the presented method has been evaluated for the detection of shear waves introduced by radiation force on a tissue-mimicking phantom. The results showed that CFWI was better able to visualize the shear wave propagation along depth and time (Figs. 5 and 6). The amplitude of the CFWI spatiotemporal map did not degrade in time as much as the TDI results. This phenomenon is explained by the fact that a logarithmic compression is used during CFWI processing. The logarithmic compression did not affect the estimation of the mechanical wave velocity. Second, the dispersion curve was estimated to evaluate the effect of CFWI on the frequency content of the detected shear waves. It was shown that CFWI could detect the shear waves up to 2.5 kHz in this example, while TDI approximately detects them up to 1.5 kHz. The improvement of the temporal resolution by CFWI can be explained by the fact that the method keeps a higher temporal frequency content of the data which will increase the temporal resolution of the wavefront. Moreover, the dispersion curves obtained with both methods presented a difference at around 400 Hz. This singularity can be due to the detection of a second mode of the shear waves by CFWI or due to the high-pass filter, which was set with a cutoff frequency at 465 Hz in this experiment.

CFWI was further evaluated *in vivo* for the detection of the PWV propagating in a carotid artery. We showed that CFWI detects the forward, reflected, and the dicrotic notch waves and gives very similar results to the results obtained with TDI. The different mechanical wave velocities were estimated using the acceleration map resulting from both approaches. We showed that the mechanical wave velocities, estimated by CFWI, were more consistent than those estimated with TDI. These results can be explained by the fact that the temporal resolution and the SNR of the slope were found superior with CFWI.

Moreover, this result showed that CFWI did not need any averaging filter to be able to detect the propagation of the PWV. Indeed, as shown in Fig. 10, the PWV estimation can depend on the spatiotemporal filtering. A larger spatiotemporal window will lead to a higher estimated mechanical wave velocity estimation in this example. As the spatiotemporal filter spreads the mechanical wavefront in space and time, it increases the speed of the wave artificially. Hence, the spatiotemporal window has to be as small as possible in order to affect as little as possible the estimation of the wave speed.

The effect of the cutoff frequency on mechanical wave velocity was studied (Fig. 11). The variation of the estimated velocity is inferior to the variation using one single cutoff frequency over 12 cardiac cycles. These results allow us to claim that the estimated PWV velocities are robust concerning the choice of cutoff velocity. Finally, the acceleration obtained by each approach were mapped onto the B-mode sequences. We showed that the PWV velocity is more accessible with CFWI. This can be explained by the fact that CFWI detected the PWV with a better temporal and spatial resolution.

Finally, CFWI was evaluated for the detection of mechanical waves propagating along the left ventricle of a healthy volunteer. For this experimentation, the maximum tissue velocity was very close to the Nyquist velocity limit. A first-order Butterworth filter with a cutoff frequency corresponding to the maximum velocity would be equivalent to a simple differentiator filter and would not give the expected results. Consequently, a third-order Butterworth filter with a cutoff frequency corresponding to half of the maximum tissue velocity was empirically chosen. For cardiac imaging, the results show that the presented method can better detect the mechanical waves around the apical region and the lateral wall than TDI. Two different factors can explain the poor quality of the results obtained with TDI. First, the poor quality of the IQ image sequences and aliasing deteriorated the velocity estimation. Better image quality and higher frame rate could allow better TDI results. Besides, if we assume that some of these waves are shear waves (propagation of motion perpendicular to the tissue, along with the tissue); both methods detect the axial component of this motion. Consequently, if the left ventricle wall is perfectly aligned with the beam axis, the detection of the mechanical waves will be more difficult. Overall, despite the poor quality of the image sequence, and the difficulty in detecting the mechanical waves in the four chambers view, CFWI gives promising results and seems to be more sensitive to small motion induced by the mechanical waves. Only the velocities of the a′ wave [Fig. 12 (2)] and AVC wave [Fig. 12 (5)] were estimated because they were the only waves detected with consistency over multiple cardiac cycles using TDI. However, the velocity of the other waves detected with CFWI can be estimated with consistency and will be investigated in future work.

Despite the promising results obtained with CFWI, the method presents three main disadvantages. The first one is related to the fact that CFWI is not able to differentiate the mechanical waves induced by a positive or negative velocity. Indeed, some of the detected mechanical waves, such as the dicrotic notch waves for the carotid or mechanical wave event (4) in Fig 12 for the left ventricle, appear with different colors in the figure. The estimation of the tissue velocity curve is then essential to understand where the mechanical waves are coming from. A potential improvement will be to use two filter operations to separate the positive and negative components.

Furthermore, as it is shown in this paper, the clutter filter cutoff and design determine the tissue velocities of interest and will need to be determined for a given application. The presented method could be further developed to adapt the cutoff frequency over time and to the estimated tissue velocity; in this way, the wave detection induced by different tissue velocities could be improved. Finally, since a possible zero-crossing from a combined rotation and translation motion is projected as a traveling wave, CFWI may give a false wave detection, if this combined motion occurs during an actual wave propagation (note that this phenomenon did not appear in our experiments).

V. Conclusion

A new method able to detect the propagation of mechanical waves in tissue without using motion estimation has been presented. The technique was evaluated for the propagation of the PWV in a carotid artery, mechanical waves in the left

ventricle, and shear waves induced by radiation forces in a tissue-mimicking phantom. The results were compared to TDI and showed that CFWI could detect the mechanical waves propagating in tissue with better consistency. On average, the relative resolution of the slope and the relative consistency of the mechanical wave velocity estimated were found to be 30% and 40% higher than for TDI, respectively. Second, the results show that CFWI could detect mechanical waves with a relative frequency content 40% higher than TDI for a shear wave imaging experiment.

REFERENCES

[1] M. Tanter and M. Fink, "Ultrafast imaging in biomedical ultrasound," *IEEE Trans. Ultrason., Ferroelectr., Freq. Control*, vol. 61, no. 1, pp. 102–119, Jan. 2014.

[2] T. A. Krouskop, D. R. Dougherty, and F. S. Vinson, "A pulsed Doppler ultrasonic system for making noninvasive measurements of the mechanical properties of soft tissue," *J. Rehabil. Res. Develop.*, vol. 24, no. 2, pp. 1–8, 1987.

[3] Y. Yamakoshi, J. Sato, and T. Sato, "Ultrasonic imaging of internal vibration of soft tissue under forced vibration," *IEEE Trans. Ultrason., Ferroelectr., Freq. Control*, vol. 37, no. 2, pp. 45–53, Mar. 1990.

[4] A. P. Sarvazyan, O. V. Rudenko, S. D. Swanson, J. B. Fowlkes, and S. Y. Emelianov, "Shear wave elasticity imaging: A new ultrasonic technology of medical diagnostics," *Ultrasound Med. Biol.*, vol. 24, no. 9, pp. 1419–1435, Dec. 1998.

[5] S. Catheline, J.-L. Thomas, F. Wu, and M. A. Fink, "Diffraction field of a low frequency vibrator in soft tissues using transient elastography," *IEEE Trans. Ultrason., Ferroelectr., Freq. Control*, vol. 46, no. 4, pp. 1013–1019, Jul. 1999.

[6] M. Couade *et al.*, "Quantitative assessment of arterial wall biomechanical properties using shear wave imaging," *Ultrasound Med. Biol.*, vol. 36, pp. 1662–1676, Oct. 2010.

[7] M. Shinohara, K. Sabra, J.-L. Gennisson, M. Fink, and M. Tanter, "Real-time visualization of muscle stiffness distribution with ultrasound shear wave imaging during muscle contraction," *Muscle Nerve*, vol. 42, no. 3, pp. 438–441, Sep. 2010.

[8] L. Zhai *et al.*, "Characterizing stiffness of human prostates using acoustic radiation force," *Ultrason. Imag.*, vol. 32, no. 4, pp. 201–213, Oct. 2010.

[9] M. L. Palmeri *et al.*, "Noninvasive evaluation of hepatic fibrosis using acoustic radiation force-based shear stiffness in patients with nonalcoholic fatty liver disease," *J. Hepatol.*, vol. 55, no. 3, pp. 666–672, Sep. 2011.

[10] C.-L. Yeh, B.-R. Chen, L.-Y. Tseng, P. Jao, T.-H. Su, and P.-C. Li, "Shear-wave elasticity imaging of a liver fibrosis mouse model using high-frequency ultrasound," *IEEE Trans. Ultrason., Ferroelectr., Freq. Control*, vol. 62, no. 7, pp. 1295–1307, Jul. 2015.

[11] P. J. Brands, J. M. Willigers, L. A. F. Ledoux, R. S. Reneman, and A. P. Hoeks, "A noninvasive method to estimate pulse wave velocity in arteries locally by means of ultrasound," *Ultrasound Med. Biol.*, vol. 24, no. 9, pp. 1325–1335, Dec. 1998.

[12] S. I. Rabben *et al.*, "An ultrasound-based method for determining pulse wave velocity in superficial arteries," *J. Biomech.*, vol. 37, no. 10, pp. 1615–1622, Oct. 2004.

[13] A. Eriksson, E. Greiff, T. Loupas, M. Persson, and P. Pesque, "Arterial pulse wave velocity with tissue Doppler imaging," *Ultrasound Med. Biol.*, vol. 28, no. 5, pp. 571–580, May 2002.

[14] C. J. Hartley, G. E. Taffet, L. H. Michael, T. T. Pham, and M. L. Entman, "Noninvasive determination of pulse-wave velocity in mice," *Amer. J. Physiol. Heart Circulatory Physiol.*, vol. 273, no. 1, pp. H494–H500, Jul. 1997.

[15] J. Luo, R. X. Li, and E. E. Konofagou, "Pulse wave imaging of the human carotid artery: An *in vivo* feasibility study," *IEEE Trans. Ultrason., Ferroelectr., Freq. Control*, vol. 59, no. 1, pp. 174–181, Jan. 2012.

[16] S. Salles, A. J. Y. Chee, D. Garcia, A. C. H. Yu, D. Vray, and H. Liebgott, "2-D arterial wall motion imaging using ultrafast ultrasound and transverse oscillations," *IEEE Trans. Ultrason., Ferroelectr., Freq. Control*, vol. 62, no. 6, pp. 1047–1058, Jun. 2015.

[17] H. Kanai, "Propagation of spontaneously actuated pulsive vibration in human heart wall and *in vivo* viscoelasticity estimation," *IEEE Trans. Ultrason., Ferroelectr., Freq. Control*, vol. 52, no. 11, pp. 1931–1942, Nov. 2005.

[18] M. Pernot, K. Fujikura, S. D. Fung-Kee-Fung, and E. E. Konofagou, "ECG-gated, mechanical and electromechanical wave imaging of cardiovascular tissues *in vivo*," *Ultrasound Med. Biol.*, vol. 33, no. 7, pp. 1075–1085, Jul. 2007.

[19] H. Kanai, "Propagation of vibration caused by electrical excitation in the normal human heart," *Ultrasound Med. Biol.*, vol. 35, no. 6, pp. 936–948, Jun. 2009.

[20] E. E. Konofagou and J. Provost, "Electromechanical wave imaging for noninvasive mapping of the 3D electrical activation sequence in canines and humans *in vivo*," *J. Biomech.*, vol. 45, no. 5, pp. 856–864, Mar. 2012.

[21] B. Brekke *et al.*, "Ultra-high frame rate tissue Doppler imaging," *Ultrasound Med. Biol.*, vol. 40, no. 1, pp. 222–231, Jan. 2014.

[22] H. J. Vos *et al.*, "Cardiac shear wave velocity detection in the porcine heart," *Ultrasound Med. Biol.*, vol. 43, no. 4, pp. 753–764, 2017.

[23] H. Kanai and M. Tanaka, "Minute mechanical-excitation wave-front propagation in human myocardial tissue," *Jpn. J. Appl. Phys.*, vol. 50, no. 7, Jul. 2011, Art. no. 07HA01.

[24] T. Gallot, S. Catheline, P. Roux, J. Brum, N. Benech, and C. Negreira, "Passive elastography: Shear-wave tomography from physiological-noise correlation in soft tissues," *IEEE Trans. Ultrason., Ferroelectr., Freq. Control*, vol. 58, no. 6, pp. 1122–1126, Jun. 2011.

[25] Y. Deng, N. C. Rouze, M. L. Palmeri, and K. R. Nightingale, "Ultrasonic shear wave elasticity imaging (SWEI) sequencing and data processing using a verasonics research scanner," *IEEE Trans. Ultrason., Ferroelectr., Freq. Control*, vol. 64, no. 1, pp. 164–176, Jan. 2017.

[26] C. Kasai, K. Namekawa, A. Koyano, and R. Omoto, "Real-time two-dimensional blood flow imaging using an autocorrelation technique," *IEEE Trans. Sonics Ultrason.*, vol. TSU-32, no. 3, pp. 458–464, May 1985.

[27] S. Langeland, J. D'hooge, H. Torp, B. Bijnens, and P. Suetens, "Comparison of time-domain displacement estimators for two-dimensional RF tracking," *Ultrasound Med. Biol.*, vol. 29, no. 8, pp. 1177–1186, Aug. 2003.

[28] F. Viola and W. F. Walker, "A comparison of the performance of time-delay estimators in medical ultrasound," *IEEE Trans. Ultrason., Ferroelectr., Freq. Control*, vol. 50, no. 4, pp. 392–401, Apr. 2003.

[29] C. Jia *et al.*, "Comparison of 2-D speckle tracking and tissue Doppler imaging in an isolated rabbit heart model," *IEEE Trans. Ultrason., Ferroelectr., Freq. Control*, vol. 57, no. 11, pp. 2491–2502, Nov. 2010.

[30] J. Luo and E. E. Konofagou, "A fast normalized cross-correlation calculation method for motion estimation," *IEEE Trans. Ultrason., Ferroelectr., Freq. Control*, vol. 57, no. 6, pp. 1347–1357, Jun. 2010.

[31] R. Nitzberg, *Adaptive Signal Processing for Radar*. Boston, MA, USA: Artech House, 1992.

[32] H. Torp, "Clutter rejection filters in color flow imaging: A theoretical approach," *IEEE Trans. Ultrason., Ferroelectr., Freq. Control*, vol. 44, no. 2, pp. 417–424, Mar. 1997.

[33] S. M. Torres and D. S. Zrnic, "Ground clutter canceling with a regression filter," *J. Atmos. Ocean. Technol.*, vol. 16, no. 10, pp. 1364–1372, Oct. 1999.

[34] E. S. Chornoboy, "Initialization for improved IIR filter performance," *IEEE Trans. Signal Process.*, vol. 40, no. 3, pp. 543–550, Mar. 1992.

[35] R. H. Fletcher and D. W. Burlage, "An initialization technique for improved MTI performance in phased array radars," *Proc. IEEE*, vol. 60, no. 12, pp. 1551–1552, Dec. 1972.

[36] L. Thomas and A. Hall, "An improved wall filter for flow imaging of low velocity flow," in *Proc. IEEE Ultrason. Symp.*, vol. 3, Oct./Nov. 1994, pp. 1701–1704.

[37] L. A. F. Ledoux, P. J. Brands, and A. P. G. Hoeks, "Reduction of the clutter component in Doppler ultrasound signals based on singular value decomposition: A simulation study," *Ultrason. Imag.*, vol. 19, no. 1, pp. 1–18, 1997.

[38] S. Bjærum, H. Torp, and K. Kristoffersen, "Clutter filter design for ultrasound color flow imaging," *IEEE Trans. Ultrason., Ferroelectr., Freq. Control*, vol. 49, no. 2, pp. 204–216, Feb. 2002.

[39] M. Bernal, I. Nenadic, M. W. Urban, and J. F. Greenleaf, "Material property estimation for tubes and arteries using ultrasound radiation force and analysis of propagating modes," *J. Acoust. Soc. Amer.*, vol. 129, no. 3, pp. 1344–1354, Mar. 2011.

[40] D. Garcia, L. L. Tarnec, S. Muth, E. Montagnon, J. Porée, and G. Cloutier, "Stolt's f-k migration for plane wave ultrasound imaging," *IEEE Trans. Ultrason., Ferroelectr., Freq. Control*, vol. 60, no. 9, pp. 1853–1867, Sep. 2013.

[41] H. Hasegawa, K. Hongo, and H. Kanai, "Measurement of regional pulse wave velocity using very high frame rate ultrasound," *J. Med. Ultrason.*, vol. 40, no. 2, pp. 91–98, Apr. 2013.